Interfacial stiffness and adhesion of randomly rough contacts probed by elastomer colloidal AFM probes

2008 J. Phys.: Condens. Matter 20 354014

(http://iopscience.iop.org/0953-8984/20/35/354014)

IOP PUBLISHING JOURNAL OF PHYSICS: CONDENSED MATTER

J. Phys.: Condens. Matter **20** (2008) 354014 (9pp) doi:10.1088/0953-8984/20/35/354014

Interfacial stiffness and adhesion of randomly rough contacts probed by elastomer colloidal AFM probes

R Buzio[1] **and U Valbusa**

Nanomed Labs, ABC—Advanced Biotechnology Center, Largo R. Benzi 10, 16136 Genova, Italy
and
Physics Department, University of Genova, Via Dodecaneso 33, 16146 Genova, Italy

E-mail: buzio@fisica.unige.it

Received 28 January 2008, in final form 19 May 2008
Published 11 August 2008
Online at stacks.iop.org/JPhysCM/20/354014

Abstract

We report on contact mechanics experiments addressing the role of surface roughness on interfacial stiffness and adhesion. Colloidal atomic force microscopy probes, based on poly(dimethylsiloxane) microparticles, are pressed against ceramic substrates with different roughnesses; the applied load, deformation rate and dwell time being separately controlled. We observe a clear dependence of load–deformation curves and pull-off forces on roughness values, likely arising from morphological modulation of the contact area; remarkably this affects the contact stiffness, which is found to decrease for rougher junctions. The emergence of purely geometrical effects for poly(dimethylsiloxane) rough contacts extends previous findings on plastically deformed self-affine surfaces and demonstrates the efficient tuning of contact response through a proper design of surface morphology.

1. Introduction

Surface roughness plays a major role in contact mechanics, with relevant implications for fundamental phenomena like adhesion, friction, wear and lubrication [1] and deep consequences on technological developments, including coatings technology and microelectromechanical systems design [2, 3]. It is well known that even a surface roughness of just few nanometers is enough to prevent the formation of an intimate contact between (elastically) hard solid surfaces, since the contact area is reduced to a small fraction of the nominal one and discrete, randomly distributed contact spots are formed; conversely the true area of contact might exceed the projected one for rough and (elastically) soft surfaces that are pulled into conformal contact by adhesion. The competition between the elastic energy and the adhesive energy stored at the contact interface dictates the magnitude of the real contact area under equilibrium conditions [4]: this point was originally addressed in macroscopic pull-off experiments recording the variation of adhesive force with roughness for a viscoelastic rubber ball squeezed against a hard substrate [5, 6]. Recently, there have been ongoing efforts to refine this simple picture in order to describe more realistic soft contacts, characterized by multi-scale fractal roughness [7], tack dependence on contact time and pressure [8] and eventually cavity nucleation [4, 7, 9]; these studies will have a significant impact for a number of emerging applications, e.g. soft lithographies, elastomer-based bioMEMS and biomimetic adhesives [4, 7, 10, 11].

It is expected that experiments conducted at the *mesoscale*, where both contact mechanics and morphological roughness are measured with nanoscale accuracy, should provide deeper insight on the behavior of rough junctions. So far, contact mechanics experiments addressing the interplay of viscoelasticity and morphological roughness at the mesoscale are still in their infancy. Few existing studies explore tack forces for relatively smooth and elastically stiff interfaces, formed by well-characterized polymers: they are conducted with sophisticated, custom-designed instruments (e.g. surface force apparatus) that often suffer from reduced flexibility in terms of testing materials and contact geometries [12–14].

Atomic force microscopy (AFM) offers the possibility of exploring mesoscale contact mechanics by performing

[1] Author to whom any correspondence should be addressed.

indentation experiments with colloidal probes. This approach, originally introduced by Ducker *et al* [15], is implemented by gluing a microsphere at the end of an AFM cantilever, then recording the interaction force between the sphere and a target surface. Colloidal probes with rigid inorganic beads (e.g. borosilicate glass) have been successfully used to measure the reduction of van der Waals adhesion due to nanoscale roughness [16], albeit with negligible deformation of the contact interface. In contrast, reports concerning poly(styrene) and poly(ethylene) probes attested interfacial *plastic failure* to occur at nanoscale asperities protruding from their surface [17, 18].

Our experimental strategy for studying the deformation and adhesion of rough contacts under *fully reversible* conditions focused on the use of poly(dimethylsiloxane) (PDMS) colloidal probes. We first prepared PDMS microparticles by water emulsification and cross-linking of a viscous prepolymer; the resulting beads were then attached to AFM cantilevers under optical microscopy using a micromanipulation stage. We tested the particle's response by acquiring load–displacement curves on $SrTiO_3$ ceramic substrates having different nanoscale roughnesses.

The present work extends our recent studies on the contact mechanics of PDMS beads pressed against smooth mica substrates [19] and provides a phenomenological description of the PDMS response in presence of interfacial roughness; from a broader perspective it complements some earlier measurements studying the role of nanoroughness for plastically deformed diamond/$SrTiO_3$ contacts [20].

2. Experimental techniques

2.1. Preparation of PDMS beads and colloidal probes

PDMS microparticles were synthesized by emulsification in water of a commercial viscous prepolymer, Sylgard 186 by Dow Corning [19]: this is supplied as a two-component kit consisting of a viscous base and a liquid curing agent. A 10:1 (by mass) mixture of base and cross-linking agent was poured on the rotating disk (1 cm diameter) of a DC motor, immersed in a 500 ml glass beaker filled with Milli-Q water and rotated at a speed of about 2000 rpm for few seconds. The beaker was then placed inside an oven and heated at 60 °C for 24 h, in order to cure the emulsified droplets to a flexible elastomer. The suspension was filtered by a 1 μm pores filter, on top of which PDMS micrometric spheres could be observed by optical microscopy; these were finally swollen in toluene (to remove the fraction of unbounded monomers and decrease bulk viscoelasticity), dried in air and heated overnight at 90 °C.

Particles of 20–30 μm diameter were manipulated using a thin tungsten wire and attached to the apex of silicon cantilevers with molten Shell Epikote resin [15]. Their surface morphology was inspected by the Dimension 3100 AFM (Digital Instruments, Veeco), operated in tapping mode: colloidal probes were placed on a silicon wafer, located by optical microscopy and scanned by sharp tips. Surface roughness, evaluated on areas of 10×10 μm^2, was typically of ∼2 nm. Scanning electron microscopy (SEM) (CrossBeam 1540 XB, Zeiss) was also used to check particles' overall shape (figure 1). We intentionally discarded colloidal probes with AFM and SEM topographies showing isolated asperities, of a few tens nanometers in size, placed on top of the contact region.

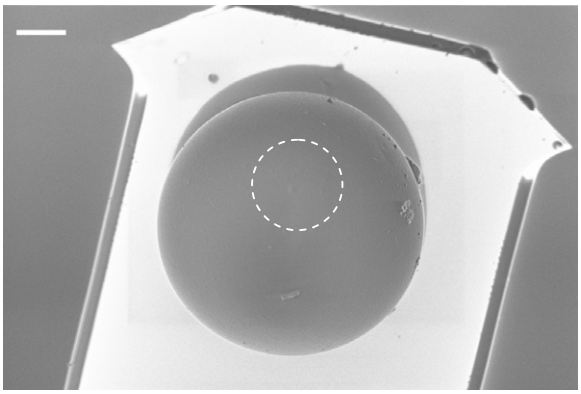

Figure 1. SEM micrograph of a PDMS bead glued to the free end of an AFM cantilever (top view; white bar corresponds to 4 μm): it shows sub-micrometric particles around the bead–cantilever contact region, that are likely to originate from the gluing process; isolated nanometric asperities are visible on the lateral surface of the bead. The contact region (roughly circled by the white dash line) is free of relevant bumps.

2.2. Preparation of substrates

The studied specimens consisted of commercial single-crystals of $SrTiO_3$ (Crystal-GmbH), commonly used as substrates for the epitaxial growth of oxides [21]: one side of each substrate is chemo-mechanically polished by the manufacturer in order to obtain an atomically smooth (001) termination, while the backside is lapped with a roughness in the micrometer range. In the following we refer to 'sample 1' and 'sample 2' to indicate two $SrTiO_3$ substrates exposing respectively the atomically smooth frontside and the micrometric rough backside to the PDMS probe. We further lapped the rough side of a third $SrTiO_3$ sample, named 'sample 3', to obtain a new surface with intermediate morphological properties with respect to samples 1 and 2: lapping was accomplished by pressing the sample against a 300 rpm rotating disk of grade 1000 sandpaper for about 30 min.

Representative AFM topographies of the three samples are shown in figures 2(a)–(c): monoatomic terraces of ∼0.4 nm height and 150–400 nm width are visible on sample 1 (figure 2(a)), whereas self-affine roughness characterizes samples 2 and 3 (figures 2(b) and (c)). Self-affinity was established by evaluation of the height–height correlation function $G(\boldsymbol{r})$, defined as $G(\boldsymbol{r}) \equiv \langle [h(\boldsymbol{r}+\boldsymbol{r}') - h(\boldsymbol{r}')]^2 \rangle$ where $h(\boldsymbol{r})$ is the surface height at position $\boldsymbol{r} = (x, y)$ and the average is extended to all possible values of $\boldsymbol{r}'$. Essentially $G(\boldsymbol{r})$ measures the lateral correlation of the surface height. For self-affine surfaces $G(\boldsymbol{r})$ is a function of the length $r = |\boldsymbol{r}|$, with asymptotic behavior $G(r) \approx r^{2\alpha}$ for $r \ll \xi$ and $G(r) \approx 2\sigma^2$ for $r \gg \xi$, where α $(0 < \alpha < 1)$ is the self-affine exponent, ξ the lateral correlation length and σ the

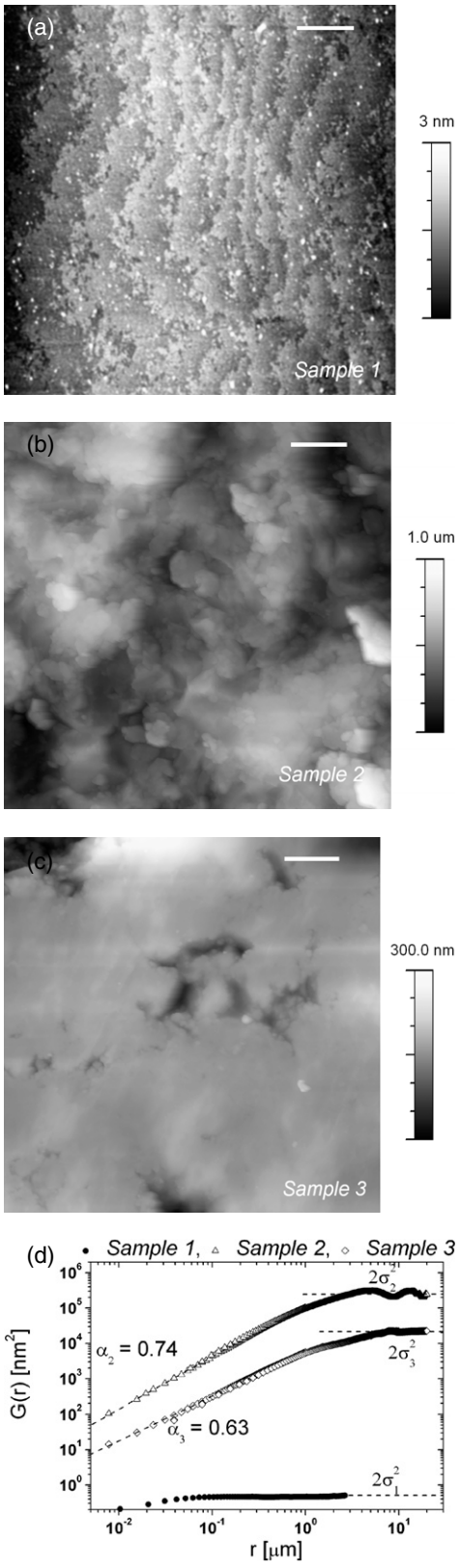

Figure 2. AFM topographies of $SrTiO_3$ single-crystal substrates: (a) chemo-mechanically polished (001) surface with monoatomic terraces (white bar corresponds to 1 μm); (b) mechanically lapped by manufacturer (as received; white bar corresponds to 5 μm); (c) mechanically lapped (white bar corresponds to 5 μm). (d) Height–height correlation function $G(r)$ for ceramic substrates: samples 2 and 3 display the power-law behavior typical of self-affine surfaces.

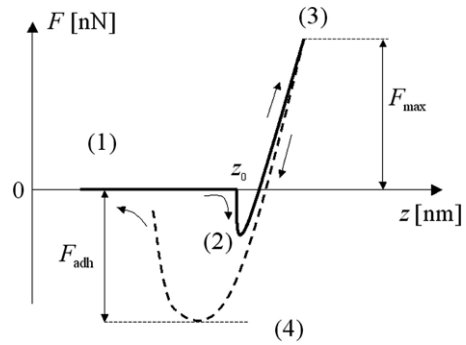

Figure 3. (a) Schematics of force–displacement curve acquired by AFM against an atomically smooth surface; the relevant contact processes are the approach (1), the adhesive jump-to-contact (2), the elastic deformation at maximum force (3) and the adhesive detachment event (4). The value of z_0, corresponding to the scanner displacement at zero tip–sample distance, is assigned at the minimum detectable attractive force recorded immediately before the 'jump-to-contact' event (see the text).

saturated surface roughness [4]. We calculated the height–height correlation function $G(r)$ using AFM topographies and averaging over several images, as explained in detail elsewhere [20]; results are reported in figure 2(d). Samples 2 and 3 display a power-law scaling $G(r) \approx r^{2\alpha}$, with $\alpha_2 \approx 0.74$ and $\alpha_3 \approx 0.63$ respectively, that proves the multi-scale, self-repeating character of roughness for $r < \xi_{2,3} \approx 1$ μm; on the contrary for $r \gg \xi_{2,3} G(r)$ achieves a constant value $\approx 2\sigma^2$, with $\sigma_2 \approx 350$ nm and $\sigma_3 \approx 106$ nm. The $G(r)$ function of sample 1 (estimated by averaging over topographies with different atomic step orientations) is constant for $r > \xi_1 \approx 0.1$ μm (figure 2(d)), as expected for a scale invariant (saturated) roughness $\sigma_1 \approx 0.5$ nm. A quantitative description of surface morphology based on the height–height correlation function $G(r)$ (or equivalently on the power spectrum) provides the necessary knowledge for the implementation of novel contact mechanics models dealing with fractal roughness [4, 7]. This approach might overcome some ambiguities related to the description of the contact interface through statistical distributions of asperity heights, or local slopes, curvatures and densities of asperities, that are in fact scale dependent quantities for most real surfaces [20]. We will attempt such a detailed study in our forthcoming investigations.

2.3. Contact mechanics AFM experiments

Contact mechanics experiments were performed at $T = 25\,^{\circ}$C in ambient air (relative humidity RH $\approx$ 40–50%), by means of the Dimension 3100 AFM equipped with a closed-loop scanner (Hybrid XYZ Scanner by Veeco; nonlinearity $\leqslant 1\%$) and operated in contact mode: to this purpose we glued PDMS beads on relatively stiff cantilevers (MikroMasch NSC35AlBS, nominal stiffness 14 N m^{-1}). Standard deflection–displacement curves were obtained by recording the cantilever deflection u (in V) while ramping the scanner displacement z (in nm). A schematic of force plots is shown for clarity in figure 3, where cantilever deflection u was

converted into *normal force* F by the Hookean relationship:

$$F = k_C S_{ph} u \tag{1}$$

with S_{ph} photodiode sensitivity (in nm V^{-1}) and k_C the measured elastic stiffness of the colloidal probe. Inspection of figure 3 allows us to understand the following events: as the scanner elongates the bead approaches the surface and finally contacts it with a 'jump-to-contact' region. The particle is then deformed until the maximum load F_{max} is applied. In the receding process a hysteresis appears because of viscoelastic energy dissipation and the particle remains adhered to the plate even at the point of zero load; when a tensile force is applied, the particle passes through the maximum adhesive interaction, where the adhesive force (or tackiness) F_{adh} is defined, and finally detachment occurs. Relevant controllable parameters of the cycle are the approaching/retracting speed V, the maximum compressive load F_{max} and the contact time t_C, separating the 'jump-to-contact' and detachment events.

Force–displacement curves can be used to study the dependence of deformation and adhesion on surface roughness provided that the photodiode sensitivity S_{ph} and the elastic constant k_C are known with sufficient accuracy. We estimated the photodiode sensitivity S_{ph} by indenting with the colloidal probe a silicon wafer close to a fracture edge, ensuring that only the very end of the cantilever was touching the surface; to measure the probe stiffness k_C we first calibrated silicon cantilevers using the analysis of Sader *et al* [22], based on measurements of lever geometry, fundamental resonance frequency and quality factor, then we estimated the effective stiffness of a colloidal probe by multiplying the elastic constant of the bare cantilever by the factor $(L_c/L_b)^3$, where L_b is the distance of the glued PDMS bead with respect to the base of the lever. Details on the implementation and precision of both methods are reported elsewhere [19].

Gaining a deeper insight on the contact mechanics process requires the conversion of force–displacement curves into force–deformation curves. The deformation δ is usually calculated as the scanner displacement minus the corresponding cantilever deflection, that is:

$$\delta = (z - z_0) - S_{ph} u \tag{2}$$

where z_0 is the scanner displacement at zero tip–sample distance. We assigned z_0 at the minimum detectable *attractive* force of the loading curve (figure 3), i.e. immediately before the 'jump-to-contact' region, and we routinely converted raw deflection–displacement curves into force–deformation curves by using equations (1) and (2). The choice for z_0, already suggested in similar studies [23], gives $\delta(z_0) = -S_{ph} u(z_0) \approx 0$, thus we are assuming that the particle is not deformed at incipient contact. We recognize that this is a questionable choice in any indentation experiment involving deformable surfaces and there is some uncertainty in the actual degree of strain of PDMS particles at z_0, since deformations might occur prior to contact due to long-range van der Waals forces; nevertheless we have to ignore such an effect, assuming that long-range deformations are considerably smaller than those induced by compressive and tensile forces during the experiment.

An important mechanical quantity, extensively considered in the following paragraph, is the *contact stiffness* $s_C \equiv dF/d\delta$, which can be expressed as:

$$s_C = k_C S_{ph} \frac{du}{dz} \frac{1}{\left(1 - S_{ph} \frac{du}{dz}\right)}. \tag{3}$$

According to equation (3), s_C can be estimated directly from deflection–displacement curves: it assumes finite values for a compliant interface for which $d\delta/dz = (1 - S_{ph}\, du/dz) > 0$, whereas $s \to +\infty$ for an infinitely stiff contact ($d\delta/dz \to 0$).

Within our experiments the deformation rates and dwell time were set using the AFM control software: in fact this allowed the separate control of the loading and unloading rate in a force–displacement cycle as well as the establishment of feedback at the maximum applied force F_{max} for a given time: the latter possibility was used to keep PDMS particles in contact with substrates for few seconds before unloading.

3. Results and discussion

Force–displacement curves reported in the following were acquired by means of a colloidal PDMS probe of bead diameter $D = (21 \pm 3)\ \mu$m and elastic constant $k_C = (51 \pm 19)$ N m^{-1}. Experiments were carried out using different PDMS particles and qualitative similar features were observed for all of them, therefore we will focus in the following, for the sake of quantitative consistency, on data obtained for the 21 μm particle.

It is well known that PDMS response during force–displacement curves is strongly affected by bulk and interfacial viscoelasticity as well as structural rearrangements occurring at the contact interface: these facts require the contact process to be probed by separately controlling the deformation rate and dwell time. We recently examined the dependence of loading–unloading cycles $F(\delta)$ and pull-off force F_{adh} on V and t_C for PDMS beads in contact with ion-sputtered mica [19], and quantified PDMS elastic modulus, interface energy and characteristic relaxation times involved in a typical AFM experiment. A similar analysis was conducted in the present case for data acquired on sample 1: this provided a framework for a comparative analysis with results of samples 2 and 3.

3.1. Loading process

The role of roughness in contact mechanics is highlighted by figures 4(a) and (b), that compare the mechanical response of PDMS on samples 1 and 2 respectively. Experimental data for sample 1 (figure 4(a)) closely resemble the schematic diagram of figure 3: on approaching the substrate a relatively sharp jump-to-contact transition takes place (within 30 nm of bead deformation) followed by a nonlinear increase of normal force F with penetration depth δ. The unloading process consists on the contrary of a linear decrease of F with δ, due to stress release within the contact junction at fixed contact area, followed by a nonlinear decrease of force associated to crack opening and detachment events [24–27]. The discontinuous character of the cycle at $F \approx F_{max}$ reflects PDMS softening over the dwell time t_C due to bulk viscoelasticity; expressions

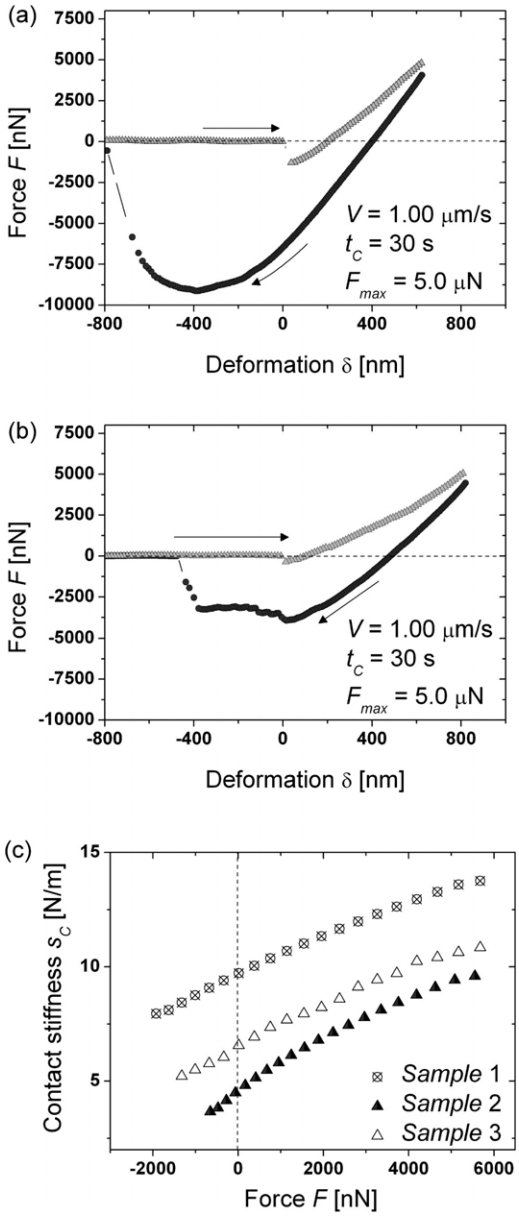

Figure 4. Experimental force–displacement curves for a PDMS colloidal probe of radius $R = 10.5\ \mu$m interacting with $SrTiO_3$ substrates. (a) Typical AFM force–displacement curve on sample 1. (b) Typical AFM force–displacement curve on sample 2. (c) Contact stiffness s_C plotted against the externally applied load F: we estimated s_C by smoothing and taking the derivatives of representative loading curves for samples 1, 2 and 3.

for the Young's modulus relaxation can be extracted from the adhesion-induced indentation curves and compared to the theoretical predictions coming from constitutive models for linear viscoelasticity, as the extended Zener model [23]. The latter indicates an exponential decrease of the PDMS elastic modulus from ∼3.4 MPa (for $t_C \to 0$ s) to ∼1.7 MPa (for $t_C \to +\infty$), with relaxation time $\tau \approx 0.4$ s [19].

Figure 4(b) demonstrates a qualitative variation of the loading cycle when roughness enters the contact interface. The jump-to-contact transition is less pronounced and occurs within 12 nm of bead deformation, due to a reduction of the van der Waals adhesive force over the geometrically rough contact interface [4]. Moreover, the maximum penetration depth at $F = 5.0\ \mu$N is $\delta_{max} = 810$ nm, i.e. 30% higher than that recorded for sample 1 under similar working conditions ($\delta_{max} = 620$ nm): this indicates that the rougher contact is more compliant than the smoother one, despite the fact that the intrinsic mechanical properties of the system remain the same. Comparison of loading curves for samples 1, 2 and 3, demonstrates a continuous variation of jump-to-contact region and repulsive forces with σ (not shown); notably, s_C at $F \approx 0$ nN increases from ∼4.5 N m^{-1} for sample 2 to ∼9.5 N m^{-1} for sample 1 (figure 4(c)). The origin of this behavior is qualitatively explained on purely geometrical grounds, by invoking the redistribution of the external load on the multiple contact junctions formed between the PDMS probe and the substrate. In fact for a given deformation δ, the rougher the substrate is, the smaller is the real contact area when pressed against the PDMS bead (for fixed load F, rougher substrates display higher penetrability). Evidence of a partial contact between PDMS beads and substrates 2 and 3 arises also from adhesion reduction, as shown in the section below.

An increased compliance for rough contacts was already reported by Buzio *et al* for the plastic flow of self-affine thin films indented by a micrometric flat AFM probe [28]: authors observed that for $\delta/\sigma < 1$ roughness drives the contact mechanics and surface stiffness s_C varies more than one order of magnitude on small but significant changes of fractal parameters D_f and roughness σ. The present measurements extend those findings to the case of reversible (viscoelastic) deformations and $\delta/\sigma \leqslant 4$.

Our findings are consistent with data reported more recently by Benz *et al* for randomly rough poly(vinylidene fluoride-trifluoroethylene) copolymer surfaces indented by a surface force apparatus [14]: in fact surfaces with roughness varying from 3 to 220 nm exhibited an almost perfect exponential repulsion with decay length *increasing* from 2.0 to 40.0 nm with surface roughness σ; this directly leads to a roughness dependent contact stiffness.

3.2. Unloading process without cracking

The dependence of contact stiffness on surface roughness is also appreciated through the analysis of the unloading process *without cracking*: this regime corresponds to stress relaxation within the contact junction at fixed contact area. Hereafter we recall that the kinetics of adherence of viscoelastic bodies can be described by fracture mechanics concepts in terms of the strain energy release rate G and the Dupré work of adhesion w_0, i.e. crack opening occurs for $G > w_0$ whereas crack closing corresponds to $G < w_0$; at equilibrium $G = w_0$ (Griffith criterion) [25, 29–31]. For a sphere of radius R in contact with a *smooth* substrate under the external load F, the dependence of load and indentation on the tip–sample contact radius a is solved by Johnson–Kendall–Roberts (JKR) theory [32], showing that:

$$\delta = \frac{a^2}{R} - \left(\frac{4\pi w_0}{3E'}\right)^{1/2} \tag{4}$$

$$F = \frac{E' a^3}{R} - (6\pi E' w_0 a^3)^{1/2} \tag{5}$$

where $E' = (4/3)[E/(1-\nu^2)]$, E and ν are the Young's modulus and Poisson's ratio of the deformable junction. Moreover G is given by:

$$G = \frac{3a^3 E'}{8\pi R^2}\left(1 - \frac{R\delta}{a^2}\right)^2. \tag{6}$$

The unloading process without cracking starts from the maximum force and contact radius, $F_{\max}$ and $a_{\max}$, and proceeds with unloading rate V until $G > w_0$. Immediately before the crack velocity $v_C = 0$ and $G = w_0$: from equation (5) we deduce that Griffith's criterion is violated when $F < F_{cr}$:

$$F_{cr} \equiv \frac{a_{\max}^3 E'}{R} - (6\pi\, a_{\max}^3 E' w_0)^{1/2}. \tag{7}$$

For $F_{cr} \leqslant F \leqslant F_{\max}$, equations (4) and (5) provide:

$$F = \frac{3a_{\max} E'}{2}\delta - \frac{a_{\max}^3 E'}{2R} \tag{8}$$

indicating that the force plot is described in this regime by a linear relationship; this is valid for δ in the range $\delta_{cr} \leqslant \delta \leqslant \delta_{\max}$, with:

$$\delta_{cr} \equiv \frac{2F_{cr}}{3a_{\max} E'} + \frac{a_{\max}^2}{3R}. \tag{9}$$

We note that the Hertz theory upon which the JKR theory is built is applicable only under the condition of $a \ll R$, which is not strictly satisfied in the present case [19]. Estimation of finite-size effects demands the introduction of corrections to the elasticity equations, as the correction factors proposed by Shull *et al* [27]. Assuming $h = 2R$ to be the thickness of the tested compliant layer (i.e. the PDMS bead diameter) and $a/h < 0.5$ to be certainly satisfied, equation (8) is replaced by:

$$F = \frac{3a_{\max} E'}{2(1 - a_{\max}/h)}\delta - \frac{a_{\max}^3 E'}{2R(1 - a_{\max}/h)}. \tag{10}$$

The quantity $k_0 \equiv 3a_{\max} E'/[2(1 - a_{\max}/h)]$ represents the contact stiffness at unloading and the whole system can be modeled by a series of two springs, the effective spring k_0 and the effective colloidal probe spring k_C respectively. Both the Young's modulus E and the maximum contact radius $a_{\max}$ can be estimated for different values of unloading velocity V and dwell time t_C by interpolating the *linear* part of the unloading process by means of equation (10), with E and $a_{\max}$ as fitting parameters.

In figure 5(a) we report the elastic modulus E and maximum contact radius $a_{\max}$ (averaged over several realizations) obtained by fitting with equation (11) the unloading curves acquired on sample 1 and plotted as a function of V (for $t_C = 30$ s, $F_{\max} = 5.0$ μN and a loading velocity of 1 μm s^{-1}): $a_{\max} \approx 3.3$–3.4 μm, $E \approx 1.6$–1.7 MPa and $k_{0,1} \approx 16.5$–18.5 N m^{-1} for V in the range 0.2–20 μm s^{-1}. In figure 5(b) we report a similar data analysis on unloading curves acquired for t_C varying in the range 2–100 s, $F_{\max} = 2.5$ μN and a loading velocity of $V = 1$ μm s^{-1}.

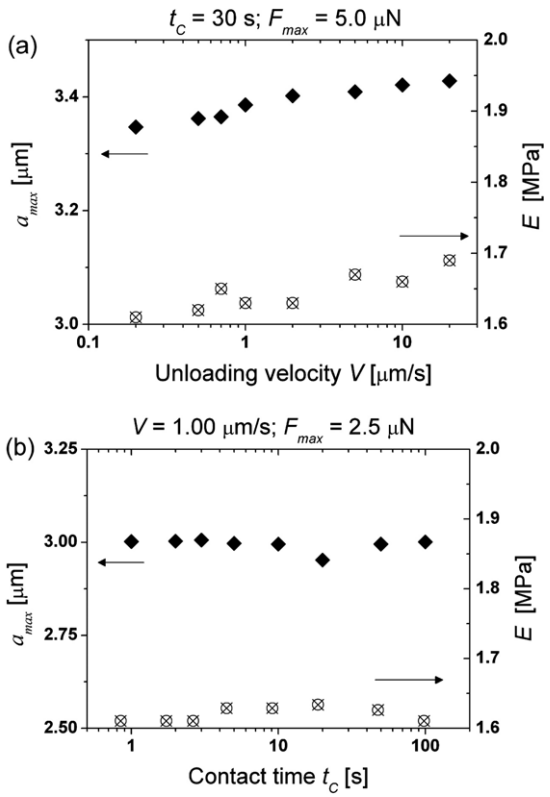

Figure 5. Data analysis of unloading curves without cracking. (a) Contact radius $a_{\max}$ and Young's modulus E obtained by linearly fitting unloading curves acquired at different deformation rates V. (b) Contact radius $a_{\max}$ and Young's modulus E obtained for different values of dwell time t_C.

It appears that the maximum contact radius remains around 3.0 μm with t_C varying over two decades, whereas the Young's modulus of the probe stays around 1.65 MPa. Experimental uncertainty on $a_{\max}$ values is of ∼5%: in fact $a_{\max}$ depends *on the ratio* of the two parameters of the linear fit, therefore it is affected only by the error on R (fitting errors are negligible). On the contrary the experimental uncertainty on E rises up to 40% due to the combination of errors on $a_{\max}$ and k_C.

Estimated values for $a_{\max}$ confirm that a *micrometric* junction is formed between the PDMS bead and the surface of sample 1; at the same time they provide an upper limit to the contact area formed with rough samples 2 and 3. The elastic modulus E is in the range of values reported for PDMS probed by macroscopic quasi-static contact mechanics experiments [33–35].

The contact mechanics of the PDMS bead with samples 2 and 3 involves formation and interaction of multiple contact spots and cannot be treated by the single-asperity JKR theory. Refined theories including multi-scale properties of surface roughness, bulk creep effects and interfacial viscoelasticity have been already reported [4, 7–9] and considerable theoretical efforts are in progress. A tight comparison of experiments with such sophisticated models demands specific design of measurements and availability of substrates with tunable roughness in a broad range of values; as mentioned above, we will attempt a similar analysis

in our forthcoming investigations. Hereafter we will adopt simple qualitative arguments to depict the phenomenology of PDMS contact mechanics in a multi-asperity regime. To this purpose we simply note that a linear relationship is found to described the force plots acquired on samples 2 and 3 (see also figure 4(b)), which allows us to define contact stiffness $k_{0,2}$ and $k_{0,3}$ respectively: we found the values $k_{0,2} \approx 10$–13 N m^{-1} and $k_{0,3} \approx 12$–15 N m^{-1} confirming the larger compliance of the rough interface with respect to the smooth one ($k_{0,1} > k_{0,2}$ and $k_{0,1} > k_{0,3}$).

3.3. Unloading process with cracking

As described in the previous paragraph, the unloading process with cracking corresponds to a monotonic reduction of PDMS/substrate contact area during the unloading ramp. Substantial differences emerge through comparison of samples 1 and 2, highlighted by figures 4(a) and (b), i.e. a decrease of adhesion force $F_{\rm adh}$ due to roughness and the occurrence of multiple elastic instabilities on the unloading curve (immediately after the adhesive peak) for sample 2. Adhesion reduction is in agreement with a relevant number of experimental investigations reported in the past [5, 6, 14, 16–18, 28] as well as with predictions of recent theoretical models [4]. Concerning the appearance of elastic instabilities, we note that their number and shape strictly depend on the specific location assumed by the PDMS bead over the indented substrate, hence their presence should be ascribed to individual detachment events occurring at isolated asperities.

As expected, we observed a remarkable dependence of the $F(\delta)$ curves on V and $t_{\rm C}$ for the smooth as well as for rough interfaces. Figures 6(a) and (b) summarize the variation of the pull-off force $F_{\rm adh}$ with unloading velocity V and dwell time $t_{\rm C}$ respectively: for simplicity we chose $F_{\rm max} = 5.0\ \mu$N and $t_{\rm C} = 30$ s in the former case, and $F_{\rm max} = 2.5\ \mu$N, $V = 1.0\ \mu$m s^{-1} for the latter. We note that $F_{\rm adh}$ separately increases with V and $t_{\rm C}$, with an overall variation of about 30%. This response is ascribed to two concomitant effects, namely the dynamic Young's modulus E increasing with V, and the appearance of an effective work of adhesion w given by the following phenomenological relationship:

$$w = w_0(t_{\rm C})[1 + f(T, v_{\rm C})] \tag{11}$$

where $f \to 0$ as $v_{\rm C} \to 0$. The $w_0(t_{\rm C})$ function shows the often-observed monotonic increase of w_0 with $t_{\rm C}$ due to the activation of the available reorganization processes of the interface upon contact [24]; the second term in the brackets indicates, on the contrary, a dependence of w on $v_{\rm C}$ arising from energy dissipation at contact edges, which has been proved experimentally by macroscale experiments [25, 27] and derived by general theoretical arguments on crack propagation in linear viscoelastic solids [36]. Therefore, the physical significance of equation (11) is that w significantly overcomes w_0 at finite values of crack velocity and dwell time.

An estimation of the most relevant parameters of the contact interface, i.e. $w_0(t_{\rm C})$ and $f(T, v_{\rm C})$, in the *absence* of roughness can be done through approximate theoretical models

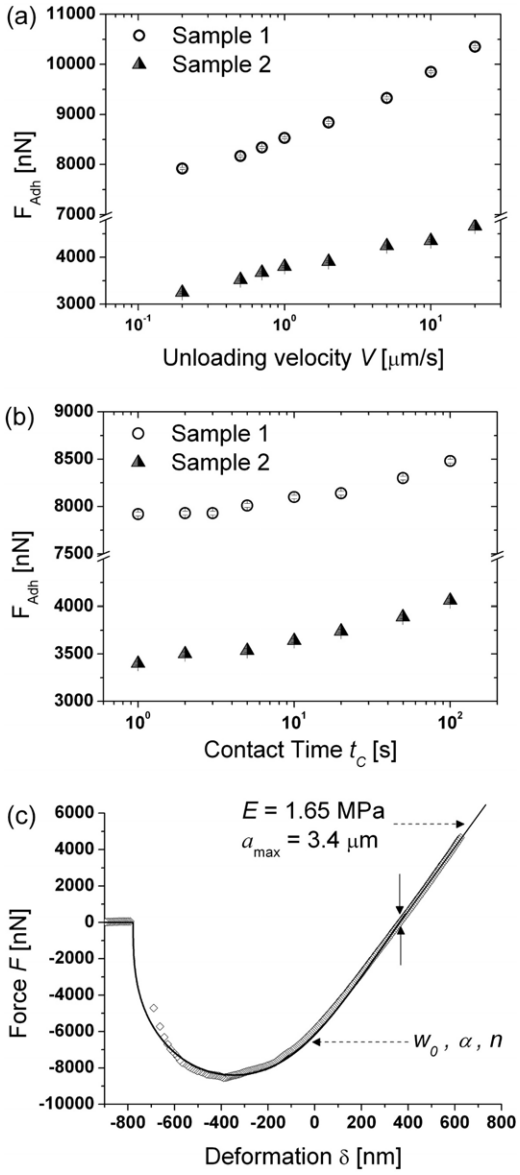

Figure 6. Experimental adhesion data for a PDMS colloidal probe of radius $R = 10.5\ \mu$m interacting with $SrTiO_3$ substrates. (a) Dependence of the adhesive force $F_{\rm adh}$ on the unloading velocity V at fixed dwell time $t_{\rm C} \approx 30$ s and maximum applied load $F_{\rm max} = 5.0\ \mu$N. (b) Dependence of the adhesive force $F_{\rm adh}$ on the dwell time $t_{\rm C}$ at fixed unloading velocity $V = 1\ \mu$m s^{-1} and maximum applied load $F_{\rm max} = 2.5\ \mu$N. (c) Comparison of representative data for sample 1 with theoretical predictions based on the Maugis–Barquins model. Arrows show the point where linear fitting, providing estimates for E and $a_{\rm max}$, is replaced by numerical integration of equations (12) and (14). The solid curve was generated for $V = 1\ \mu$m s^{-1}, $t_{\rm C} = 30$ s, with the following combination of parameters: $w_0(30) = 52$ mJ m^{-2}, $n = 0.36$, $\alpha = 250$ (s/m)$^{0.4}$.

(e.g. the Maugis–Barquins model [25]) and is reported in detail in [19]. To this purpose we simply recall that the Maugis–Barquins model assumes $f(T, v_{\rm C}) = \alpha(T)v_{\rm C}^n$: the parameter $\alpha(T)$ is related to the Williams–Landel–Ferry shift factor a_T of the elastomer by $\alpha(T) = a_T^n$, where $n \approx 0.6$ based on macroscale peeling experiments of rubber-like materials. The

crack velocity v_C is thus given by:

$$v_C = \left|\frac{da}{dt}\right| = \left(\frac{G - w_0(t_C)}{\alpha w_0(t_C)}\right)^{1/n} = \frac{1}{\alpha^{1/n}}\left[\frac{3a^3E'}{8\pi R^2 w_0(t_C)}\left(1 - \frac{R\delta}{a^2}\right)^2 - 1\right]^{1/n}. \quad (12)$$

In case of an indentation device with infinite stiffness (i.e. $k_C \gg k_0$) the time evolution of indentation is simply:

$$\delta(t) = \delta_{cr} - Vt \quad (13)$$

which can be inserted into equation (11). The latter can be solved numerically with standard techniques, since the involved parameters and initial conditions are known.

In contrast, for a finite stiffness indentation device (i.e. $k_C \approx k_0$), the deformation and unloading rates are related by (see equations (1), (2) and (13)):

$$\frac{d\delta}{dt} = V - \frac{1}{k_C}\frac{dF}{dt} = \frac{1}{1 + \frac{3}{2}\frac{aE'}{k_C}}\left[V - \frac{3E'}{2k_C}\left(\delta - \frac{a^2}{R}\right)\frac{da}{dt}\right]. \quad (14)$$

Equations (12) and (14) are coupled and can be solved iteratively as shown by Barquins and Maugis [37]: this predicts the unloading curve from crack opening up to the final separation.

In order to implement the Maugis–Barquins model for load-deformation curves acquired on sample 1, the Young's modulus E and maximum contact radius a_{max} were chosen according to figure 5, and the remaining *three* unknown parameters, $w_0(t_C)$, n and α, were arbitrarily chosen and used to calculate F_{cr} and δ_{cr} (from equations (7) and (9)) as well as to predict the whole force plot for $F < F_{cr}$ (by numerically solving equations (12) and (14) with a fourth order Runge–Kutta method); the generated curve was then compared with the experimental one by visual inspection and $w_0(t_C)$, n and α were adjusted to minimize the difference between experimental and predicted values.

In figure 6(c) we compare an experimental unloading curve acquired on sample 1 at $V = 1\ \mu m\ s^{-1}$ and $t_C = 30$ s with theoretical curves obtained by numerical integration of Maugis–Barquins theory: the two vertical arrows denote the starting point of numerical predictions, that is (δ_{cr}, F_{cr}) given by equations (7) and (9). Agreement within 10% between theory and experiment was always found for $V = 0.1$–$10\ \mu m\ s^{-1}$ by choosing the three parameters in the range $w_0(30) = 50$–$55\ mJ\ m^{-2}$, $n = 0.35$–0.38 and $\alpha = 210$–$260\ (s\ m^{-1})^{0.4}$; such values are negligible affected by the introduction of finite-size correcting factors into equations (12) and (14) (see [19]).

Figures 6(a) and (b) demonstrate that interfacial viscoelastic losses and surface rearrangements are not significantly affected by the transition from a single-asperity contact to a multi-asperity one, and we conclude that our estimates for $w_0(t_C)$, n and α can also be safely used to describe the isolated junctions at the PDMS/sample 2 interface.

For completeness we recall that $w_0(t_C)$ and $f(T, v_C)$ in equation (11) can also be estimated using a new model recently proposed by Greenwood and Johnson [26]: in such a case $f(T, v_C)$ is related to the creep compliance function of a standard linear 'three-element' solid, having a single creep time constant τ. Through interpolation of representative data we estimated $\tau \approx 1.2 \times 10^{-5}$–$1.5 \times 10^{-5}$ s for PDMS beads [19], not too far from the creep time constant $\approx 10^{-6}$ s found by Wahl *et al* for unfilled PDMS films by depth-sensing nanoindentation under oscillatory loading conditions [38]. This complements the loading curves analysis previously reported (section 3.1), which indicates that a longer time constant $\tau \approx 0.4$ s dominates Young's modulus relaxation.

4. Conclusions

In summary, we addressed the role of surface roughness on interfacial stiffness and adhesion by investigating the deformation of PDMS colloidal AFM probes in contact with $SrTiO_3$ substrates with different roughnesses.

The observed phenomena are well described as follows: (i) loading–unloading curves depend on interfacial roughness both qualitatively and quantitatively; (ii) contact stiffness remarkably decreases for rougher contacts due to morphological modulation of contact area; (iii) adhesion force is significantly reduced on rougher contacts; (iv) viscoelastic losses and structural rearrangements at the PDMS/$SrTiO_3$ interface are not appreciably affected by contact geometry. These points support the growth of a phenomenological framework for the contact mechanics of elastically soft, rough surfaces and sustain efforts aiming at validating contact mechanics theories at the mesoscale.

Acknowledgments

The authors thank Giuseppe Firpo and Luca Repetto for SEM imaging and all of the members of the ESF program NATRIBO for comments. This work was supported by the Italian Ministry of University and Research MIUR within the project FIRB 'NanoMed'.

References

[1] Bowden F P and Tabor D 1954 *Friction and Lubrication of Solids* (London: Oxford University Press)
[2] Assender H, Bliznyuk V and Porfyrakis K 2002 *Science* **297** 973
[3] Bishop D, Gammel P and Giles C R 2001 *Phys. Today* **54** 38
[4] Persson B N J, Albohr O, Tartaglino U, Volokitin A I and Tosatti E 2005 *J. Phys.: Condens. Matter* **17** R1
[5] Briggs G A D and Briscoe B J 1977 *J. Phys. D: Appl. Phys.* **10** 2453
[6] Fuller K N G and Roberts A D 1981 *J. Phys. D: Appl. Phys.* **14** 221
[7] Persson B N J 2006 *Surf. Sci. Rep.* **61** 201
[8] Creton C and Leibler L 1996 *J. Polym. Sci.* B **34** 545
[9] Chiche A, Pareige P and Creton C 2000 *C. R. Acad. Sci. Paris* IV **1** 1197
[10] Geim A K, Dubonos S V, Grigorieva I V, Novoselov K S, Zhukov A A and Shapoval S Y 2003 *Nat. Mater.* **2** 461
[11] Majidi C, Groff R E, Maeno Y, Schubert B, Baek S, Bush B, Maboudian R, Gravish N, Wilkinson M, Autumn K and Fearing R S 2006 *Phys. Rev. Lett.* **97** 76103

[12] Falsafi A, Deprez P, Bates F S and Tirrell M 1997 *J. Rheol.* **41** 1349
[13] Ruths M and Granick S 1998 *Langmuir* **14** 1804
[14] Benz M, Rosenberg K J, Kramer E J and Israelachvili J N 2006 *J. Phys. Chem.* B **110** 11884
[15] Ducker W A, Senden T J and Pashley R M 1991 *Nature* **353** 239
[16] Drelich J 2006 *Miner. Metallurg. Proc.* **23** 226
[17] Reitsma M, Craig V and Biggs S 2000 *Int. J. Adhes. Adhes.* **20** 445
[18] Tormoen G W and Drelich J 2005 *J. Adhes. Sci. Technol.* **19** 181
[19] Buzio R, Bosca A, Krol S, Marchetto D, Valeri S and Valbusa U 2007 *Langmuir* **23** 9293
[20] Buzio R and Valbusa U 2006 *Applied Scanning Probe Methods III* ed B Bhushan and H Fuchs (Heidelberg: Springer) p 261
[21] Kawasaki M, Takahashi K, Maeda T, Tsuchiya R, Shinohara M, Ishiyama O, Yonezawa T, Yoshimoto M and Koinuma H 1994 *Science* **266** 1540
[22] Sader J E, Chon J W N and Mulvaney P 1999 *Rev. Sci. Instrum.* **70** 3967
[23] Sun Y and Walker G C 2005 *Langmuir* **21** 8694
[24] Vakarelski I U, Toritani A, Nakayama M and Higashitani K 2001 *Langmuir* **17** 4739
[25] Maugis D and Barquins M 1978 *J. Phys. D: Appl. Phys.* **11** 1989
[26] Greenwood J A and Johnson K L 2006 *J. Colloid Interface Sci.* **296** 284
[27] Shull K L 2002 *Mater. Sci. Eng.* R **36** 1
[28] Buzio R, Boragno C, Biscarini F, Buatier de Mongeot F and Valbusa U 2003 *Nat. Mater.* **2** 233
[29] Greenwood A G and Johnson K L 1981 *Phil. Mag.* A **43** 697
[30] Hui C Y, Baney J M and Kramer E J 1998 *Langmuir* **14** 6570
[31] Barthel E 1998 *J. Colloid Interface Sci.* **200** 7
[32] Johnson K L, Kendall K and Roberts A D 1971 *Proc. R. Soc.* A **324** 301
[33] Chaudhury M K and Whitesides G M 1991 *Langmuir* **7** 1013
[34] Chaudhury M K and Owen M J 1993 *Langmuir* **9** 29
[35] Pickering J P, Van Der Meer D W and Vancso G J 2001 *J. Adhes. Sci. Technol.* **15** 1429
[36] Carbone G and Persson B N J 2005 *Eur. Phys. J.* E **17** 261
[37] Barquins M and Maugis D 1981 *J. Adhes.* **13** 53
[38] Wahl K J, Asif S A S, Greenwood J A and Johnson K L 2006 *J. Colloid Interface Sci.* **296** 178